Journal of Materials Chemistry A

ROYAL SOCIETY OF CHEMISTRY

PAPER

View Article Online
View Journal

Cite this: DOI: 10.1039/d6ta00538a

Improved electrocatalytic oxidation of artificial seawater with an applied magnetic field in a forward osmosis system

Jayeeta Saha,[a] Tushar Kanta Sahu,[a] German Salazar Alvarez[b] and Mats Johnsson*[a]

Received 20th January 2026
Accepted 15th March 2026

DOI: 10.1039/d6ta00538a

rsc.li/materials-a

It is desirable to be able to use seawater directly for electrocatalytic splitting and hydrogen production. However, challenges such as electrode corrosion and chlorine gas evolution limit its practical application. In this study, a transition metal-based phosphide/phosphate (Ni–NiPO) catalyst on Ni foam was developed to improve charge transfer and suppress parasitic reactions. To improve stability and selectivity, a chloride ion-selective forward osmosis (FO) membrane was integrated into the system, which effectively minimised chlorine oxidation and corrosion. The FO membrane exhibited excellent stability (48 hours) and OER selectivity at pH 8. In addition, the application of a 100 mT magnetic field improved the OER kinetics, reducing the overpotential from 0.45 V to 0.31 V. It is shown that the combination of the Ni–NiPO catalyst, FO membrane and an applied magnetic field significantly improves the control of the OER.

Introduction

Rising concerns over environmental pollution and the global energy crisis have driven significant efforts toward developing clean and sustainable energy sources. Among these, hydrogen stands out as an abundant, renewable, and clean fuel, making it a highly promising alternative to fossil fuels. One of the most environmentally friendly and sustainable approaches for large-scale hydrogen production is electrocatalytic water splitting.[1] Achieving an efficient hydrogen evolution reaction (HER) and oxygen evolution reaction (OER) during electrocatalysis with a minimal overpotential is critical for advancing water-splitting technologies and reducing the amount of electricity consumed.[2–5] The energy required to conduct the four main stages (production, storage, safety, and utilisation) should be reduced for an economically viable hydrogen economy. Energy is needed for water purification and reaction activation for the production stage in the H_2 economy. The aim is to use substantially less energy for the overall process compared to the energy content of the produced H_2. To stimulate the reaction, energy is needed in terms of overpotential, which can come either from conventional energy (fossil fuel) or alternative energy (wind, solar, or hydro) for the HER or OER.[6] Due to the slow kinetics, the OER requires a large overpotential that significantly hinders the overall efficiency.[1,7] So, to reduce the overpotential of the electrocatalytic reaction, modification of the electrocatalyst and electrolytes is often approached. While iridium- and ruthenium-based catalysts are currently considered the most effective and stable for the OER, their large-scale application is hindered by limited availability and high cost. Consequently, designing cost-effective, high-performance OER electrocatalysts derived from earth-abundant elements has become an urgent priority.[8] Transition metal (TM)-based oxides/phosphides have been regarded as the most promising OER electrocatalysts due to their unfilled 3d orbitals, low cost, and relatively high efficiency. However, a relatively large overpotential is still required by the OER, even when using TM-based electrocatalysts.[8,9] This indicates that substantial improvements cannot be achieved solely through the design and regulation of electrocatalyst materials. To push beyond these intrinsic material limitations, the introduction of external stimuli has emerged as a promising strategy. Stimuli such as visible light, magnetic fields, and heating can provide additional driving forces that enhance charge transfer, accelerate reaction kinetics, and influence spin selection during catalytic processes.[10,11] In particular, light-assisted catalysis (photoelectrocatalysis) can not only supply extra energy to lower activation barriers but also promote the generation of energetic charge carriers, thereby synergistically improving reaction efficiency.[12,13] Similarly, magnetic and electric fields can modulate the spin states of intermediates and tune the electronic structure of active sites, which is especially relevant for reactions governed by spin selection rules.[11] Within this framework, the spin-sensitive nature of the OER is particularly noteworthy. Since the OER involves the conversion of singlet-state reactants (OH^- or H_2O) into triplet-state O_2 molecules, spin selection becomes a critical factor in determining the overall reaction

[a]Department of Chemistry, Stockholm University, Stockholm, Sweden. E-mail: mats.johnsson@su.se
[b]Department of Material Science and Engineering, Ångström Laboratory, Uppsala University, Uppsala, Sweden

rate. Recent studies have highlighted that aligning the spin states of intermediates can significantly reduce kinetic barriers, thereby improving catalytic efficiency.[14] This has led to a growing interest in spintronic approaches to catalysis, where magnetic interactions are intentionally harnessed to optimize electrocatalytic performance.

One major problem with electrocatalysis, which is usually neglected, is the availability of fresh water for efficient splitting. As freshwater accessibility is low, the potential of direct use of seawater should be further explored as a source of clean energy. Due to the relatively small potential difference between the OER and oxidation of chlorine ions unwanted chlorine oxidation reactions may take place at the anode to form hypochlorite or hypochlorous acid.[15,16] In addition, Cl^- ions can accelerate electrode degradation through corrosion or by directly reacting with catalyst surfaces, forming unstable metal chloride–hydroxide layers. These processes diminish the catalytic performance. To address this issue, conventional approaches rely on freshwater purification, which itself requires substantial energy input, undermining the overall sustainability and economic feasibility of hydrogen production. Other than this, several strategies have been explored: operating in alkaline media to improve OER selectivity, designing chloride-resistant catalysts, and employing protective or selective membrane technologies. Hybrid approaches, such as integrating forward osmosis (FO) membranes or seawater reverse osmosis (SWRO) with electrolysis, can provide desalinated water directly to the electrolyzer, bypassing energy-intensive purification steps while mitigating chloride-related side reactions.[17,18] Recent research highlights that combining material design with system-level solutions, including pH control, membrane architecture, and catalyst engineering, offers a practical pathway toward sustainable, large-scale seawater electrolysis for clean hydrogen production.[19–21] FO membranes can effectively desalinate seawater before it enters the electrolyzer, thereby mitigating Cl^--induced side reactions and corrosion. This hybrid FO-electrolysis approach not only bypasses the need for energy-intensive water purification steps but also improves the long-term stability and efficiency of large-scale electrolyzer setups, ultimately enhancing economic viability.

In this study, we explore a solution to tackle some of the problems outlined above. Two visions are integrated: (i) an application viewpoint: electrocatalytic water splitting with catalysts responding to a magnetic field, and (ii) a technical outlook: a FO membrane coupled to a water electrolysis cell to directly use desalinated water for splitting. We report an efficient and robust nickel phosphide/phosphate catalyst to achieve stable artificial seawater oxidation with an overpotential of 310 mV in 1 M phosphate buffer at pH 8 under a magnetic field of 100 mT.

Experimental

Preparation of the Ni–NiO electrode

Ni–NiO electrodes were fabricated on Ni-foam substrates using a hydrothermal method. Prior to fabrication, the Ni-foam was first ultra-sonicated in deionised water for 10 min followed by acetone for 10 min. For the synthesis of NiO, 2 mmol $Ni(NO_3)_2 \cdot 6H_2O$ (Merck, 97%), 20 mmol $CO(NH_2)_2$ (Merck) and 0.5 mmol $[(C_{16}H_{33})N(CH_3)_3]Br$ (CTAB) (Merck, ≥98%) were dissolved in 20 mL of deionised water, followed by ultrasonic treatment for 30 minutes. The solution was then transferred to a 50 mL Teflon-lined autoclave containing Ni-foam and heated at 120 °C for 6 h. A precipitate then formed on the Ni-foam, which was further calcined at 450 °C for 2 h to obtain nanostructured NiO deposited on the Ni-foam (Ni–NiO) electrodes.[22]

Preparation of the Ni–NiPO electrode

For the phosphidation step, 0.2 g $NaH_2PO_2 \cdot H_2O$ (≥99%, Merck) was used in a furnace with an upstream Ar flow at 300 °C for 2 h to convert nickel oxide to phosphides and form a Ni–NiPO electrode. During heat treatment, $NaH_2PO_2 \cdot H_2O$ releases PH_3, which acts as a phosphorus source that reacts with the oxide and hydroxide precursors.[23,24]

Material characterization

Powder X-ray diffraction (PXRD) data were obtained using a Bruker D8-Discover X-ray diffractometer with Cu K_α radiation to identify the crystalline phases in the samples. The morphology of the catalyst materials on the electrodes was characterised using a field-emission scanning electron microscope (FE-SEM) (JSM-7000F, JEOL) and transmission electron microscope (TEM) (JEM-2100F, JEOL). The elemental composition and distribution were investigated with an energy dispersive X-ray spectrometer (EDS) attached to a JSM-IT800 (JEOL) instrument. High Angle Annular Dark Field-Scanning Transmission Electron Microscopy (HAADF-STEM) images and Energy Dispersive X-ray Spectroscopy (EDS) elemental mapping were obtained on a Thermo Fisher Scientific Themis Z microscope operating at 300 kV equipped with a SuperX EDS detector. X-ray photoelectron spectroscopy (XPS) (Phi Quantera II) was carried out to analyse the chemical composition and valence states of the constituent elements in the samples. The spectrometer was equipped with an Al K_α source and operated at 15 kV with a total power of 50 W. A pass energy of 224 eV was used to measure the survey spectra, while a pass energy of 55 eV was used to measure high-resolution XPS spectra. All XPS spectra were calibrated with C 1s high-resolution spectra, and the backgrounds were removed using the Shirley method. The binding energies for the Ni 2p high resolution spectra ($2p_{1/2}$ and $2p_{3/2}$), O 1s spectra and P 2p spectra are in accordance with the reported studies.[25–28]

The UV-visible absorption spectra of the resulting solutions were recorded using an Agilent Cary 5000 UV/Vis/NIR spectrophotometer. Fluorescence spectroscopy was performed using a Varian Cary Eclipse fluorescence spectrophotometer. The phosphate concentration in the artificial seawater, chloride concentration in the electrolyte and hypochlorite concentration formed due to chloride oxidation in the electrolyte were determined using a method reported by Veroneau *et al.*[15,29]

Electrochemical measurements

The electrochemical properties were measured at room temperature in a standard three-electrode set-up using an SP-50e potentiostat (Biologic). The catalyst electrodes were used as working electrodes. Ag/AgCl and platinum electrodes were

used as the reference and counter electrodes, respectively. The electrolytes for the OER analysis were 1 M phosphate buffer with different pH (pH 6, 7 and 8). The linear sweep voltammetry (LSV) curves were collected at a scan rate of 5 mV s^{-1}. The *iR* drop for the LSV curves was directly compensated by the potentiostat at 85%, and the compensated resistance was about 2 to 3 Ω. LSV curves were obtained after 50 cycles of CV to activate the catalysts. Potentiostatic electrical impedance spectroscopy (PEIS) was conducted at a constant potential in the frequency range of 200 kHz to 100 mHz, and fitted using Zfit software. The potentials recorded from electrochemical tests were calibrated to the reversible hydrogen electrode (RHE) by using the equation: $E_{RHE} = E_{Ag/AgCl} + 0.059 \times pH$. The overpotential of the OER (η_{OER}) was calculated using the equation: $\eta_{OER} = E_{RHE} - 1.23$. The η_{OER} was calculated at a current density of 10 mA cm^{-2} for all the experiments. The electrochemical active surface area (ECSA) of an electrode was estimated by using the equation: $ECSA = C_{dl}/C_S$, where C_{dl} is the electrochemical double-layer capacitance and is calculated by measuring the non-faradaic capacitive current from the scan-rate dependent cyclic voltammetry (CV) curves. C_S is the specific capacitance for a flat surface; the reported C_S is generally 30 μF cm^{-2}. The ECSA was used to normalise the current and C_{dl}. The stability of the catalysts was observed by conducting chronoamperometry and chronopotentiometry for 36–48 h. Prior to electrochemical measurements, the electrolyte was purged with N_2 gas to remove dissolved oxygen present in the electrolyte.

Preparation of a forward osmosis membrane coupled water splitting (FOWS) cell

A forward osmosis cell (FOWS) was constructed by connecting a 50 mL plastic centrifuge tube containing the electrolyte consisting of 1 M phosphate buffer (pH 6, 7 and 8), in which the electrolysis takes place with a three-electrode configuration (WE, RE and CE) and an external solution of artificial seawater containing 0.5 M NaCl solution. The two solutions were in contact *via* a commercially available forward osmosis (FO) membrane made of cellulose triacetate from STERLITECH (FTSH2O Flat Sheet Membrane). The membrane has limited functionality at pH values higher than 7.

Magneto-electrochemical measurements

Neodymium-based permanent disk magnets of radius 25 mm and thickness 10 mm were placed outside the electrocatalytic setup. Two such magnets were placed opposite to each other on the circumference of the electrocatalytic cells, resulting in a magnetic field of 100 mT at the centre of the cell. The magnetic field was measured using a Gauss meter (ZMST-5 Digital Tesla meter). The magnetic field was applied perpendicular to the electric field.

Results and discussion

Morphology and phase composition

Nanoflakes of nickel oxide/hydroxide were synthesised on Ni-foam using a hydrothermal technique (hereafter named Ni–NiO), see Fig. 1a, S1 and S2. Subsequently, the nickel oxide/hydroxide nanoflakes were partially converted into nickel phosphides and phosphates (hereafter named Ni–NiPO) during phosphidation in a tube furnace at elevated temperature. The morphology transformed from nanoflakes to layered nanoparticles (Fig. 1b). The presence and homogeneous distribution of Ni, P, and O are confirmed from EDS mapping and from EDS spectra (Fig. S3 and S4).

The Ni–NiPO sample was further investigated by use of transmission electron microscopy (TEM). Low-resolution TEM images show a similar morphology to what is observed in SEM (Fig. 1c: inset). High-resolution TEM reveals interplanar distances of 0.19, 0.22 and 0.24 nm, which can be attributed to the (201), (111), and (211) planes, respectively, of the Ni_2P phase (Fig. 1c). The SAED pattern shows (111), (201), and (211) planes of the Ni_2P phase (Fig. 1d), in agreement with previous studies of Ni_2P.[30,31] High-angle annular dark-field scanning TEM (HAADF-STEM) clearly shows formation of nickel phosphide nanoflakes (Fig. 1e). Energy-dispersive X-ray spectrometry mapping shows a relatively homogeneous distribution of oxygen, indicating the presence of phosphates.

The powder X-ray diffraction (PXRD) pattern of Ni–NiO agrees with the diffraction files of NiO (PDF 47-1049) and β-$Ni(OH)_2$ (PDF 14-0117), see Fig. S5.[32,33] The diffraction peaks at 2θ = 20.6, 28.6, 37.6, and 63.3° can be indexed to the (001), (100), (101), and (111) planes of NiO, respectively, and the 2θ = 37.6, 43.7, and 63.3° can be indexed to the (101), (200), and (111) planes of β-$Ni(OH)_2$, respectively, along with the 2θ peaks of Ni-foam at 44.5° (111) and 51.9° (200).[25]

After phosphidation, the PXRD pattern of Ni–NiPO shows Ni_2P (PDF 04-003-1863) with the diffraction peaks at 2θ = 40.9, 45.6, 47.6, 52.6, 53.1, and 59.3° indexed to the (111), (201), (210), (110), (300), and (211) planes, respectively.[34] Also, the presence of nickel phosphates is observed in the Ni–NiPO catalyst. Several broad diffraction peaks match with the phosphate phases of $Ni_2(PO_3)_4$ (PDF 01-076-1557), $Ni_2P_2O_7$ (PDF 04-014-1816) and $Ni_3(PO_4)_3$ (PDF 00-035-0987).[35] Thus, a partial conversion of oxides and hydroxides to phosphates occurs along with the formation of nickel phosphide (Ni_2P) during phosphidation, see Fig. 2a.

Furthermore, from Raman spectroscopy, it is observed that in Ni–NiO, four Raman scattering peaks are present at 510, 742, 1085, and 1490 cm^{-1}, that can be ascribed to the first-order longitudinal optical (LO1) phonon mode of the Ni–O lattice vibration, the second-order transverse (TO2), the second-order longitudinal optical (LO2) phonon modes, and the two-magnon (2 M) mode of the NiO, respectively (Fig. S6a) in accordance with the peak assignments by Terlemezoglu *et al.*[36] Only non-stoichiometric NiO shows the LO1 mode indicating the presence of defects, such as nickel vacancies. Raman spectra of crystalline Ni_2P are often weak or silent in the typical 100–1000 cm^{-1} range because Ni–P modes couple poorly to Raman scattering. Instead, the peaks observed usually correspond to oxide species or their electrochemical transformations.[37] In addition to Ni_2P, weak P–O–P (799 cm^{-1}) and P–O (1159 cm^{-1}) peaks are also observed in the Ni–NiPO electrocatalyst, confirming the presence of phosphates (Fig. S6b).[35]

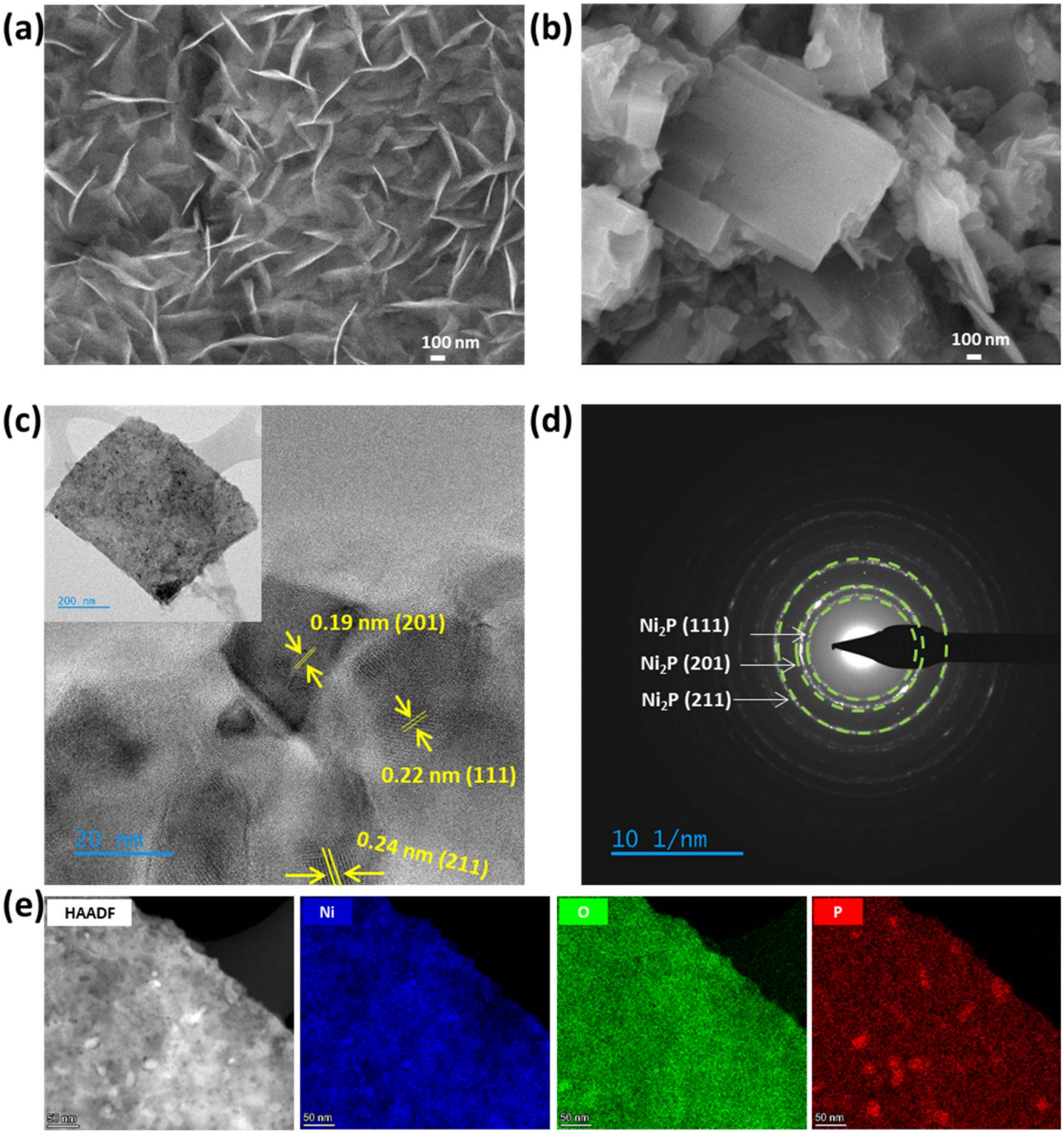

Fig. 1 SEM images of (a) Ni–NiO and (b) Ni–NiPO. (c) HRTEM images of Ni–NiPO. (d) SAED patterns of Ni–NiPO. (e) HAADF-STEM image and EDS mapping of Ni–NiPO.

XPS characterisation

The surface oxidation states and electronic structure of the catalysts were analysed using X-ray photoelectron spectroscopy (XPS). All XPS spectra were calibrated using C 1s high-resolution spectra, and the backgrounds were removed using the Shirley method. As shown in Fig. S7, the survey spectrum of Ni–NiO shows Ni 2p and O 1s, and for Ni–NiPO, P 2p is also observed. The Ni 2p high-resolution spectra for Ni–NiO are well-fitted with two spin–orbit doublets, $2p_{1/2}$ (872 eV) and $2p_{3/2}$ (854 eV), considering the 2 : 1 area proportion for the spin-split to $2p_{3/2}$ and $2p_{1/2}$, as well as shakeup satellites (860.6 and 879.6 eV), see Fig. 2c. Both doublets are peak-fitted into the oxidation states of Ni: +3 for 855.4 and 873.2 eV; and +2 for 853.8 and 871.2 eV. Similarly, the O 1s spectra of the Ni–NiO precursor, in Fig. 2d, can also be fitted to two species, which include metal-oxide-bound species (529.2 eV) (lattice oxygen: O_L), and oxygen vacancies on the surface (530.8 eV) (O_V). For Ni–NiO, O_L and O_V are observed, confirming the formation of the Ni–O bond and Ni–OH bond.

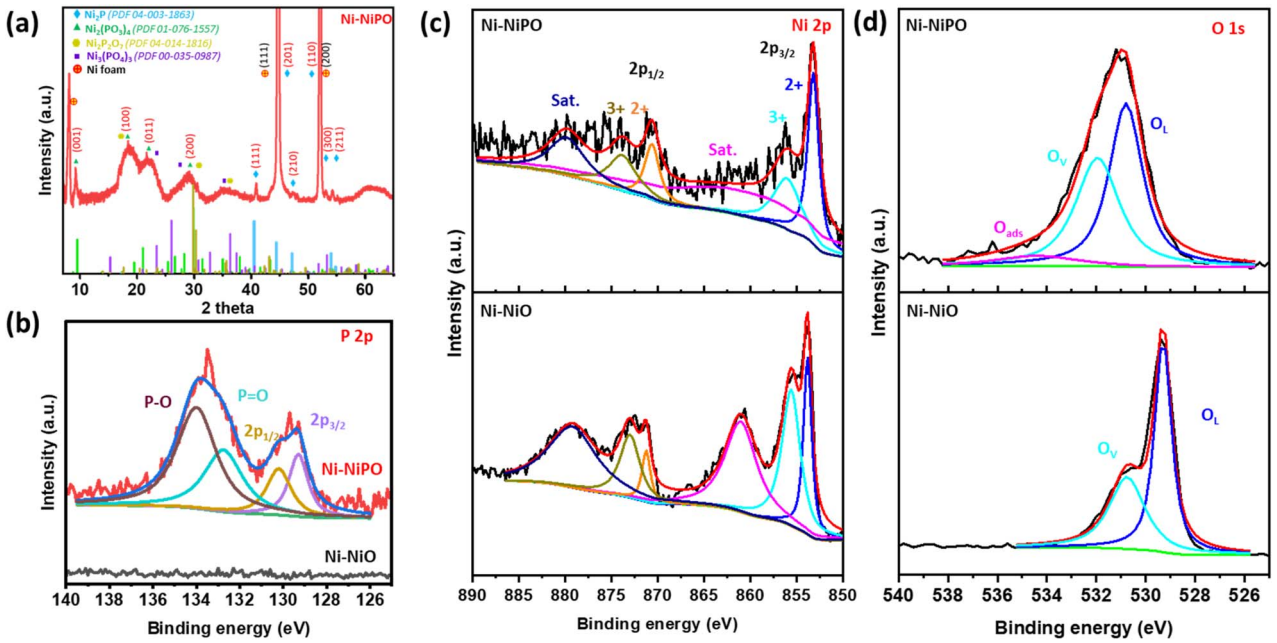

Fig. 2 (a) Powder X-ray diffraction pattern of Ni–NiPO. Deconvoluted high-resolution XPS spectra of Ni–NiO and Ni–NiPO: (b) P 2p, (c) Ni 2p, and (d) O 1s.

After thermal treatment with $NaH_2PO_2 \cdot H_2O$, the surface chemistry of the resulting Ni–NiPO was probed with XPS. The +3 state of both Ni $2p_{3/2}$ and Ni $2p_{1/2}$ comprises a higher binding energy shift (0.6 eV) in the peak position due to surface oxidation after phosphidation, with a partially charged $Ni^{\delta+}$ ($0 < \delta < 2$). The partially charged metal ions help to attain prompt electron transfer ability. It promotes more oxygen vacancies, which improve the –OH adsorption at the electrode surface. Along with this, the increased intensity of +2 states of both Ni $2p_{3/2}$ and Ni $2p_{1/2}$ proves the phosphide formation from the oxides. The O 1s core-level XPS spectra of Ni–NiPO can be divided into three peaks centred at 529.2 (O_L), 532.0 (O_V), and 534.8 eV, which can be attributed to adsorbed oxygen and hydroxide species as well as P–O components.[38] An increase in the binding energy of O 1s electrons typically indicates the presence of other atoms or groups (here, phosphorus) in the molecule and molecular geometry. Again, an increase in oxygen vacancies (O_V) is observed for Ni–NiPO compared to Ni–NiO, which refers to the presence of oxygen vacancies in a material, particularly in catalysts. These vacancies are defects in the lattice structure of metal oxides or other compounds containing oxygen. They are formed during synthesis at elevated temperatures and reducing atmospheres and play a crucial role in the stability, diffusivity, and catalytic activity of the material. The P 2p region clearly represents two different environments around phosphorus (Fig. 2b): metal phosphide (P $2p_{3/2}$ = 129.2 eV and P $2p_{1/2}$ = 130.2 eV) and oxidised phosphate species P=O (132.8 eV) and P–O (134 eV) on the surface. The binding energy of P 2p of Ni–NiPO is negatively shifted from that of elemental P (130.2 eV), which suggests a partial negative charge (δ^-) on the P atom. The peak at 134 eV is attributed to an oxidised form of P atoms resulting from surface oxidation of the phosphide phase to phosphates.

Electrocatalytic performance

Electrocatalytic OER in a three-electrode setup in 1 M phosphate buffer electrolyte. To evaluate the electrocatalytic activity, the OER was first performed in an oxygen saturated 1 M phosphate buffer at pH 6, 7, and 8, using the catalyst Ni–NiPO. Linear sweep voltammetry (LSV) was performed with a conventional three-electrode setup followed by measurements in the forward osmosis cell (FOWS) (Fig. 3a), using the same setup as in our previous work.[39] From the initial LSV measurements, the overpotentials were observed to be 950, 580, and 450 mV at pH 6, 7, and 8, respectively (Fig. 3b). The lowest overpotential is thus observed at pH 8 as alkaline electrolytes provide stabilisation of key intermediates due to the presence of hydroxide ions. The Tafel slopes, calculated from the LSV measurements, are 133, 86 and 77 mV dec^{-1} for pH 6, 7, and 8, respectively, reflecting the improved charge-transfer kinetics (Fig. S8).

Electrocatalytic OER with the FOWS setup. The next step was to use the FOWS setup, as our aim is to utilize seawater for electrocatalytic water oxidation. The FOWS cell was equipped with a three-electrode setup, and the concentration of the electrolyte was chosen to compensate for the influx provided by the high surface area of the forward osmosis membrane. In the FOWS experiments, an external vessel containing 0.5 M NaCl solution (artificial seawater, 0.5 M NaCl = 3.5 wt% NaCl) was in contact with the electrochemical cell containing the phosphate buffer solution *via* a forward osmosis membrane.[39] LSV measurements were carried out over time at three different pH levels (Fig. 3c). It is observed that the overpotentials increased after 1 and 2 h at pH 6 and 7, whereas at pH 8 the overpotential remains almost the same during 2 h (Fig. 3d and Table S1). The overpotential values are calculated after repeating the experiments three times. Along with the lowest overpotential, Ni–

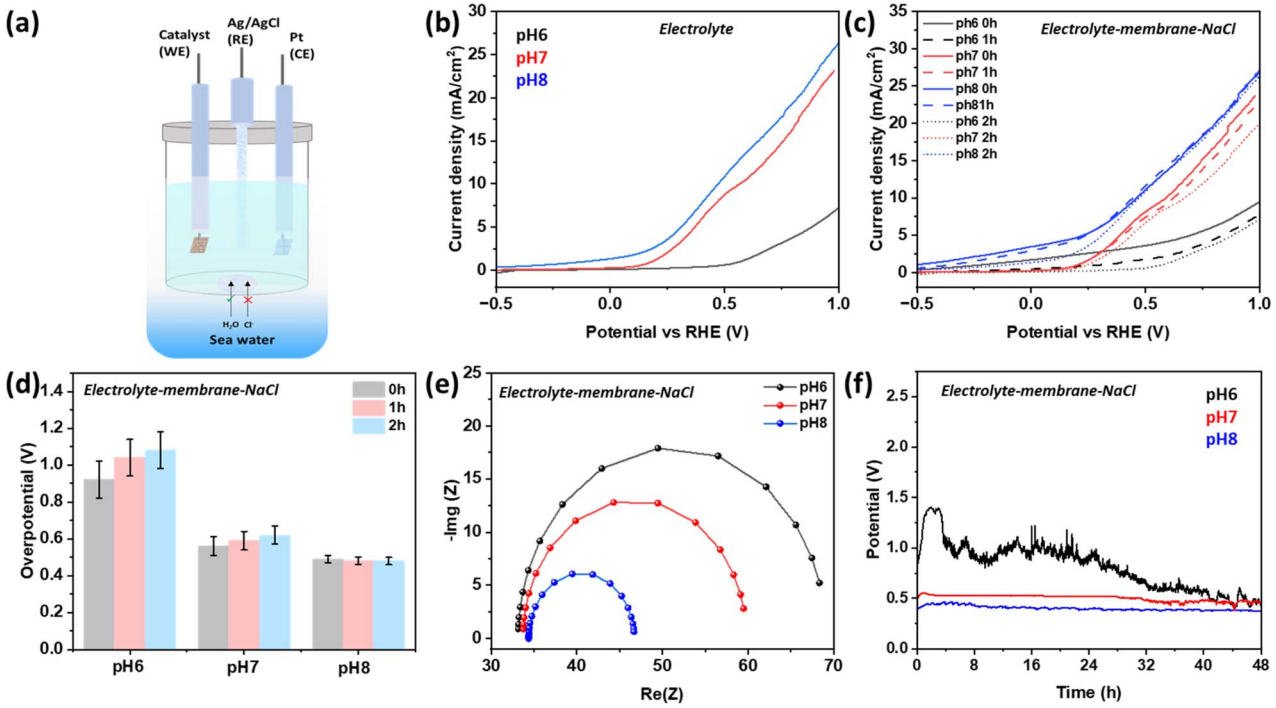

Fig. 3 Electrochemical performance of the Ni–NiPO catalyst in 1 M phosphate buffer (pH 6, 7 and 8). (a) Schematic diagram of the FOWS setup. (b) Linear sweep voltammetry of Ni–NiPO with a conventional three-electrode setup. (c) Linear sweep voltammetry after different contact times of the Ni–NiPO catalyst with the electrolyte using the FOWS setup. (d) Overpotential of the Ni–NiPO catalyst after different contact times in the FOWS setup. (e) Impedance spectroscopy: Nyquist plots of Ni–NiPO with the FOWS setup. (f) Chronopotentiometry of Ni–NiPO with the FOWS setup.

NiPO is the least affected at pH 8. To understand the interfacial interaction, impedance spectroscopy was carried out in 1 M phosphate buffer at different pH levels. Nyquist plots for Ni–NiPO show that the decrease in Re (Z) happens rapidly with an increase in pH (Fig. 3e). The charge-transfer resistance (R_{ct}) is the smallest at pH 8 (12.3 ohm) and highest at pH 6 (35.9 ohm). Also, from the Nyquist plot, the double-layer capacitance (C_{dl}) was calculated for the electrolyte 1 M phosphate buffer (Table S2). The C_{dl} increases as the pH increases from pH 6 (0.8 mF) to pH 8 (1.0 mF). The C_{dl} was used to evaluate the electrochemically active surface area (ECSA) of Ni–NiPO, as C_{dl} is directly proportional to ECSA. To evaluate the stability, chronopotentiometry was also performed at 10 mA applied current. At pH 7 and 8, the potential reached up to 0.44 V and 0.52 V, respectively, with consistency for 48 hours (Fig. 3f). But in the case of pH 6, the achieved potential is initially high (1.36 V) and not so stable over time, indicating corrosion of the Ni-electrode. The incorporation of a semipermeable FO membrane markedly suppresses the concentrations of chloride and its oxidation products, thereby minimizing their accumulation on both anode and cathode surfaces. This improvement is primarily attributed to the effective rejection of Cl^- ions *via* forward osmosis, the reduced operational potential required for the OER, and the employment of sodium phosphate as the electrolyte, which serves as a superior promoter of the OER relative to the ClOR. Owing to its selective ion exclusion properties and minimal leaching through the FO membrane, sodium phosphate represents an optimal inner electrolyte for FOWS cells operating under near neutral conditions.

Electrocatalytic OER in artificial seawater + 1 M phosphate buffer. In a third setup, it was found that during electrolysis of artificial seawater (0.5 M NaCl) + 1 M phosphate buffer, the performance is not affected at pH 8 (Fig. 4a). However, the stability of the OER at pH 6 and 7 ceases after 3 and 9 hours, respectively. The overpotential for the OER at pH 8 is much lower compared to that at pH 6 and 7 and the stability was intact during the testing period of 48 hours. Since the overpotential at pH 8 is low, the risk for the ClOR is also lower compared to that at pH 6 and 7 where the overpotential is closer to the ClOR oxidation potential, which may disrupt a stable chronoamperometric behaviour due to corrosion of the catalyst. It is thus clear that the FO membrane plays a crucial role in the setup where the artificial seawater is separated from the phosphate buffer *via* the FO membrane by selectively transporting water molecules while effectively blocking the migration of chloride ions. This selective ion transport is important because it suppresses unwanted corrosion of the electrode surface, which otherwise occurs when electrodes are directly exposed to artificial seawater.[16]

Electrocatalytic OER in artificial seawater with the FOWS setup in the presence of a magnetic field. Recently, we have established that the effect of a magnetic field (B = 100 and 200 mT) can enhance the OER efficiency using mixed metal phosphides (NiCoP and NiCoFeP).[40] Inspired by those results, we

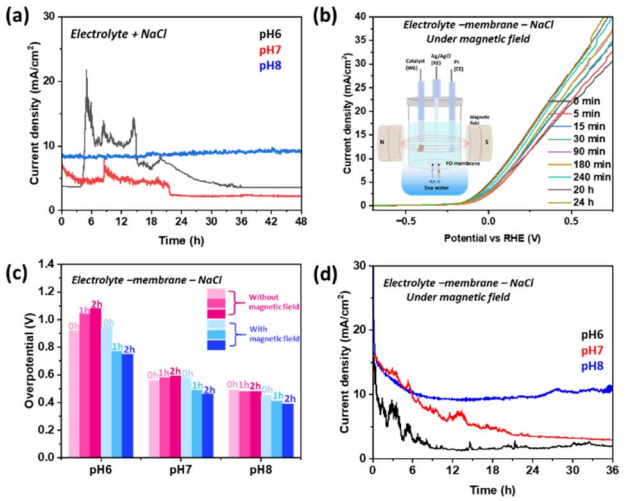

Fig. 4 (a) Chronoamperometry for the OER with the Ni–NiPO catalyst in 1 M phosphate buffer + 0.5 M NaCl at pH 6, 7 and 8 without the FOWS setup. (b) Linear sweep voltammetry of Ni–NiPO in 1 M phosphate-buffer (pH 8) with the FOWS setup under a magnetic field with time (inset: schematic diagram for the FOWS setup with a magnetic field). (c) Comparison of overpotential of the Ni–NiPO catalyst in 1 M phosphate buffer (pH 6, 7 and 8) at different time intervals (0, 1, and 2 h) with the FOWS setup with (blue) and without (pink) a magnetic field. (d) Chronoamperometry for the OER with the Ni–NiPO catalyst in 1 M phosphate buffer at pH 6, 7 and 8, under a magnetic field ($B = 100$ mT) with the FOWS setup.

applied a magnetic field of 100 mT in parallel with the electric field, for the present catalyst also in the FWOS cell for the electrocatalytic OER process.

The LSVs were acquired after different times up to 24 h to evaluate the effect of an applied magnetic field ($B = 100$ mT) at pH 6, 7 and 8 (Fig. 4b and S9). It is observed that the overpotential is lowered in the presence of a magnetic field, and with time, the overpotential decreases for all three pH values used. The overpotential achieved after applying a magnetic field for 24 hours at pH 8 (310 mV) is the lowest compared to that at pH 7 (390 mV) and pH 6 (620 mV) (Fig. S10 and Table S3). The differences with and without an applied magnetic field (100 mT) in the FOWS setup were investigated, and the overpotential was measured after different times, see Fig. 4c. With time, a lowering of the overpotential is observed when a magnetic field is applied, while the overpotential increases with time without an applied magnetic field (Table S1 and S3). The results indicate that it takes a relatively long time for the magnetic domains to align when a magnetic field is applied. Tafel slopes are calculated from the LSVs in Fig. 4b. They show a gradual decrease from 80 to 42 mV dec^{-1}, explaining the improvement in the kinetics in the presence of a magnetic field (Fig. S11). Impedance spectroscopy was performed at pH 8 in a FOWS setup under a magnetic field. From the Nyquist plot, it is observed that the R_{ct} decreases with time in the presence of a magnetic field, $B = 100$ mT (Fig. S12 and Table S4). The R_{ct} decreases to 11 ohm from 14.9 ohm after 15 minutes of magnetic field application and reaches 7.7 ohm after 60 minutes. It reflects the influence of the magnetic field in enhancing the conductivity during the electrocatalytic OER. As an external stimulus, a magnetic field enhanced the efficiency of electrocatalysis and the water splitting process can be kinetically enhanced. The electrocatalytic effects associated with the applied magnetic field are explained by the magneto-hydrodynamic effect, spin selection, and magneto-resistance.[11,41–44] This occurs due to the (i) magneto-hydrodynamic effect; as the magnetic field is placed perpendicularly to the electric field, the Lorentz force creates and removes gas bubbles at the electrode surface, (ii) higher conductivity as the magnetic domains of the catalyst gets aligned in the presence of a magnetic field to reduce the resistivity (observed in the trend of charge-transfer resistance) to enhance the mass-transport of the reaction, and (iii) spin-modification for the spin-dependent reactions like the OER; the magnetic field helps to align the spin of the oxygen radical to initiate an O–O bond easily.[14] These are the reasons responsible for improvement of the catalytic activity in the presence of a magnetic field.

To evaluate the stability of the Ni–NiPO catalyst in a FOWS setup when applying a magnetic field, chronoamperometry was performed (Fig. 4d). In the electrolyte with pH 8, the current density is observed to be stable during a 36 h experiment at 10 mA cm^{-2}, while at pH 6 and pH 7, the current density decreases with time. Furthermore, the stability was studied for 6 days in 1 M phosphate buffer at pH 6, 7 and 8, showing a stable performance (Fig. S13). It is observed that the current density is very stable at pH 8, while the current density is unstable at pH 6 and 7.

Electrocatalytic OER in 1 M phosphate buffer in the presence of a magnetic field. The magneto-electrocatalytic OER in 1 M phosphate buffer (pH 6, 7 and 8) was also performed without the FOWS setup, (Fig. S14). The change in overpotential is similar to the overpotential drop while performing the experiment in saline water with the FOWS setup under a magnetic field ($B = 100$ mT) (Table S5). This implies that FOWS helps to achieve a similar performance to what is observed when there is no contact with salt water.

The leaching of Cl^- and Na^+ ions into the electrolysis cell and leakage of phosphate out from the cell through the FO membrane is crucial during long-term runs. To have a better understanding of these properties, spectrophotometric analysis was performed to determine any probable leakages, following previous studies.[15,39] The concentrations of chloride ions (Fig. S15) and their oxidation products (Fig. S16) were measured in the inner electrolyte chamber through fluorescence spectroscopy and UV-visible spectroscopy, respectively. Along with that, the concentration of phosphate leaching through the FO membrane in the outer electrolyte was measured with UV-visible spectroscopy (Fig. S17). As observed, the phosphate leaching is around 0.1 mmol after 48 h at pH 6, which is around 0.5% of the content in the electrolyte. However, at pH 7 and pH 8, the phosphate leaching is around 1.1 mmol (5.5% of the electrolyte) and 1.2 mmol (6% of the electrolyte), respectively, after 48 h. This is mainly due to the operating limitations of the FO membrane. The amount of chloride in the electrolyte was *ca.* 42 mmol at pH 6 (8.4% of the artificial seawater), 51 mmol at pH

7 (10.2% of the artificial seawater) and 58 mmol at pH 8 (10.4% of the artificial seawater) after 48 h of continuous operation. The increase in chloride concentration with increasing pH is also due to the pH dependent operational limitations of the FO membrane. However, these influxes are ~10% of the chloride ions from the artificial seawater and the electrocatalysts are thus less exposed to chloride ions with an FO membrane as compared to direct seawater splitting. The chloride oxidation products, such as HOCl/OCl^-, produced during the continuous operation were evaluated to be *ca.* 0.21 mmol at pH 6, 0.17 mmol at pH 7, and 0.14 mmol at pH 8. With increasing pH, the oxidation products decrease as the overpotential needed for water oxidation also decreases.

Characterization after electrocatalysis experiments

Characterization studies of Ni–NiPO using SEM, XRD, and XPS were performed after chronoamperometry for 48 hours in 1 M phosphate buffer electrolyte at different pH values. SEM shows that the morphology of Ni–NiPO changes after the OER in 1 M phosphate buffer (pH 6), see Fig. S18. In contrast, the morphology of the same catalyst is fairly intact after reaction at pH 8. XRD also clearly shows that after reaction at pH 6, the phosphide phase has mainly been converted to oxides. However, Ni–NiPO that reacts at pH 8 shows low oxidation, and the Ni_2P phase is still present, see Fig. S19. XPS was performed after the OER, see Fig. S20–S23, and an increase in the binding energy of Ni 2p is observed due to the presence of oxygen on the surface of the material. The high-resolution P 2p spectra lack the P $2p_{1/2}$ and P $2p_{3/2}$ peaks for the catalyst after use at pH 6 and pH 7, while they are present at pH 8. This indicates the stability of Ni–NiPO after 48 hours of electrocatalysis at pH 8, as P 2p HRXPS shows intact P $2p_{1/2}$ and P $2p_{3/2}$ peaks together with P–O and P═O as P 2p. However, in the case of pH 6 and 7, the absence of P $2p_{1/2}$ and P $2p_{3/2}$ supports the chronoamperometric data in Fig. 4d, where the stability of the catalyst at pH 8 is superior to that at pH 6 and 7 due to degradation of the phosphide phase during electrocatalysis. Along with this, the high-resolution deconvoluted Ni 2p spectra show a disappearance of the +2 state peak after use at both pH 6 and pH 7, confirming oxidation of the catalyst. However, at pH 8, the +2 states of Ni 2p coexist with the +3 states after the OER, indicating a better stability of the catalyst. After electrochemistry, the O 1s peak appeared at 535 eV at pH 8, indicating the presence of strongly bound physisorbed oxygen species.

Conclusions

Ni-based phosphide catalysts synthesised on Ni foam and integrated with forward osmosis membranes are shown to be a promising method for direct seawater splitting. Powder X-ray diffraction and X-ray photoelectron spectroscopy verify the formation of nickel phosphide and phosphate phases from an oxide precursor. However, the conversion is not complete and oxide and hydroxide phases also remain after phosphidation. An electrocatalytic cell is designed with a chloride-ion-selective forward osmosis membrane to improve performance and durability by preventing chlorine oxidation and electrode corrosion.

The forward osmosis membrane effectively suppresses chloride ion transport while enabling rapid water transfer, reducing electrode corrosion. The best performance was achieved at pH 8, where the FO membrane offered superior stability over 48 h and high selectivity for the OER compared to the ClOR in saline environments. In addition, the application of an external magnetic field (~100 mT) improves the oxygen evolution reaction by lowering the overpotential from 0.45 V to 0.31 V and promoting the reaction kinetics.

After 48 hours of continuous operation, phosphate leaching is approximately 1.2 mmol (6% of the inner electrolyte) at pH 8, and chloride accumulation reached approximately 85 mmol. The observed increase in chloride accumulation with rising pH can be attributed to the pH-dependent operating limitations of the FO membrane. Despite this, the chloride influx remains around 10% of the total chloride ion concentration in the artificial seawater (outer electrolyte). By mitigating electrode degradation and reducing the chlorine evolution reaction (ClOR) as well as lowering the required overpotential through the synergistic application of magnetic and electric fields, this work presents a compelling strategy for the development of efficient and sustainable seawater-splitting systems.

Furthermore, the FOWS cell with the nickel phosphide/phosphate/oxide catalyst outperforms most recently reported electrocatalysts for the OER in neutral seawater (see Table S6). Continued research with different electrolytes and buffer systems may further improve performance by increasing ion selectivity and reducing electrolyte transfer. In addition to the performance and durability of the anode materials, the stability and catalytic activity of the cathode are equally important for efficient water splitting. It is worth noting that the use of an FOWS cell reduces precipitation on the cathode surface, as demonstrated in the study by Veroneau *et al.*[15] Furthermore, the efficiency of the water oxidation process can be improved by utilizing a superior membrane with better durability across the pH scale.

Author contributions

The manuscript was written through contributions of all authors. All authors have given approval to the final version of the manuscript. JS, TKS and MJ have designed the project and performed the synthesis, phase characterization and electrochemical measurements. JM and GSA have performed the XPS characterization.

Conflicts of interest

There are no conflicts to declare.

Data availability

Primary experimental data used in the study is available upon request to the corresponding author. That is *e.g.* experimental data from the characterization methods used. Supplementary

information (SI): characterization of Ni–NiO and Ni–NiPO and electrochemical measurements. See DOI: https://doi.org/10.1039/d6ta00538a.

Acknowledgements

The authors acknowledge the use of the EM facilities and the assistance of Dr Anumol Ashok at the Electron Microscopy Center at Stockholm University as well as Dr José Montero for assistance with collecting the XPS data. Olle Engkvist foundation (grant 233-0263) is acknowledged for funding.

References

1 B. H. R. Suryanto, Y. Wang, R. K. Hocking, W. Adamson and C. Zhao, *Nat. Commun.*, 2019, **10**(1), 1–10, DOI: 10.1038/s41467-019-13415-8.
2 C. Mohapatra, S. Ayushi, R. Sarma, A. Sharma, S. S. Meena, P. M. Pataniya, C. K. Sumesh and N. K. Prasad, *Ceram. Int.*, 2025, **51**, 52649–52661, DOI: 10.1016/j.ceramint.2025.09.022.
3 H. K. Thakkar, K. H. Modi, K. K. Joshi, G. Bhadu, S. Siraj, P. Sahatiya, P. M. Pataniya and C. K. Sumesh, *ACS Sustainable Chem. Eng.*, 2024, **12**, 8340–8352, DOI: 10.1021/acssuschemeng.4c00591.
4 S. V. Chauhan, K. K. Joshi, P. M. Pataniya, P. Sahatiya, G. Bhadu and C. K. Sumesh, *Renew. Energy*, 2025, **24**, 122370, DOI: 10.1016/j.renene.2025.122370.
5 N. A. Trivedi, P. J. Sharma, K. K. Joshi, V. Patel, C. K. Sumesh and P. M. Pataniya, *Int. J. Hydrogen Energy*, 2024, **61**, 1212–1219, DOI: 10.1016/j.ijhydene.2024.03.050.
6 R. D. L. Smith, M. S. Prévot, R. D. Fagan, S. Trudel and C. P. Berlinguette, *J. Am. Chem. Soc.*, 2013, **135**(31), 11580–11586, DOI: 10.1021/ja403102j.
7 S. Kundu, B. Malik, D. K. Pattanayak and V. K. Pillai, *ACS Appl. Mater. Interfaces*, 2017, **9**(44), 38409–38418, DOI: 10.1021/acsami.7b09601.
8 M. J. Craig, G. Coulter, E. Dolan, J. Soriano-López, E. Mates-Torres, W. Schmitt and M. García-Melchor, *Nat. Commun.*, 2019, **10**(1), 1–9, DOI: 10.1038/s41467-019-12994-w.
9 J. Wang, L. Gan, W. Zhang, Y. Peng, H. Yu, Q. Yan, X. Xia and X. Wang, *Sci. Adv.*, 2018, **4**(3), 1–9, DOI: 10.1126/sciadv.aap7970.
10 C. Ding, J. Shi, Z. Wang and C. Li, *ACS Catal.*, 2017, **7**(1), 675–688, DOI: 10.1021/acscatal.6b03107.
11 F. A. Garcés-pineda, M. Blasco-ahicart, D. Nieto-castro, N. López and J. R. Galán-mascarós, *Nat. Energy*, 2019, **4**, 519–525, DOI: 10.1038/s41560-019-0404-4.
12 J. Yu, J. González-Cobos, F. Dappozze, P. Vernoux, A. Caravaca and C. Guillard, *Green Chem.*, 2024, **26**, 1682–1709, DOI: 10.1039/d3gc03371f.
13 D. Liu, X. Wan, T. Kong, W. Hanc and Y. Xiong, *J. Mater. Chem. A*, 2022, **10**, 5878–5889, DOI: 10.1039/d1ta08252c.
14 C. A. Mesa, F. A. Garcés-Pineda, M. García-Tecedor, J. Yu, B. Khezri, S. Plana-Ruiz, B. López, R. Iturbe, N. López and S. Gimenez, *APL Energy*, 2024, **2**(1), 016106, DOI: 10.1063/5.0179761.
15 S. S. Veroneau, A. C. Hartnett, A. E. Thorarinsdottir and D. G. Nocera, *ACS Appl. Energy Mater.*, 2022, **5**(2), 1403–1408, DOI: 10.1021/acsaem.1c03998.
16 S. Dresp, F. Dionigi, M. Klingenhof and P. Strasser, *ACS Energy Lett.*, 2019, **4**(4), 933–942, DOI: 10.1021/acsenergylett.9b00220.
17 G. S. Cassol, C. Shang and A. K. An, *Nat. Commun.*, 2024, **15**, 2617, DOI: 10.1038/s41467-024-46964-8.
18 J. Guo, Y. Zheng and Z. Hu, *Nat. Energy*, 2023, **8**, 264–272, DOI: 10.1038/s41560-023-01195-x.
19 W. Yu, Z. Zhang and F. Luo, *Nat. Commun.*, 2024, **15**, 10220, DOI: 10.1038/s41467-024-54514-5.
20 M. A. Blommaert, D. Aili, R. A. Tufa, Q. Li, W. A. Smith and D. A. Vermaas, *ACS Energy Lett.*, 2021, **6**(7), 2539–2548, DOI: 10.1021/acsenergylett.1c00618.
21 G. Liu, Y. Xu, T. Yang and L. Jiang, *Nano Mater. Sci.*, 2023, **5**, 101–116, DOI: 10.1016/j.nanoms.2020.12.003.
22 T. H. Ko, K. Devarayan, M. K. Seo, H. Y. Kim and B. S. Kim, *Sci. Rep.*, 2016, **6**, 1–9, DOI: 10.1038/srep20313.
23 L. Ji, J. Wang, X. Teng, T. J. Meyer and Z. Chen, *ACS Catal.*, 2020, **10**(1), 412–419, DOI: 10.1021/acscatal.9b03623.
24 J. Li, J. Li, X. Zhou, Z. Xia, W. Gao, Y. Ma and Y. Qu, *ACS Appl. Mater. Interfaces*, 2016, **8**(17), 10826–10834, DOI: 10.1021/acsami.6b00731.
25 X. Hu, X. Tian, Y. W. Lin and Z. Wang, *RSC Adv.*, 2019, **9**(54), 31563–31571, DOI: 10.1039/c9ra07258f.
26 M. Cheng, H. Fan, Y. Song, Y. Cui and R. Wang, *Dalton Trans.*, 2017, **46**(28), 9201–9209, DOI: 10.1039/c7dt01289f.
27 J. T. Ren, L. Chen, H. Y. Wang, W. W. Tian, X. L. Song, Q. H. Kong and Z. Y. Yuan, *ACS Catal.*, 2023, **13**(14), 9792–9805, DOI: 10.1021/acscatal.3c01885.
28 K. H. Modi, P. M. Pataniya, S. Siraj, P. Sahatiya, V. Patel and C. K. Sumesh, *J. Energy Storage*, 2023, **63**, 107040, DOI: 10.1016/j.ceramint.2025.09.022.
29 S. S. Veroneau and D. G. Nocera, *Proc. Natl. Acad. Sci. U. S. A.*, 2021, **118**, e2024855118, DOI: 10.1073/pnas.2024855118.
30 C. Du, L. Yang, F. Yang, G. Cheng and W. Luo, *ACS Catal.*, 2017, **7**(6), 4131–4137, DOI: 10.1021/acscatal.7b00662.
31 J. Bian and C. Sun, *Adv. Energy Sustain. Res.*, 2021, **2**(6), 1–8, DOI: 10.1002/aesr.202000104.
32 S. Rakshit, S. Ghosh, S. Chall, S. S. Mati, S. P. Moulik and S. C. Bhattacharya, *RSC Adv.*, 2013, **3**(42), 19348–19356, DOI: 10.1039/c3ra42628a.
33 Z. Wu, X. L. Huang, Z. L. Wang, J. J. Xu, H. G. Wang and X. B. Zhang, *Sci. Rep.*, 2014, **4**, 3669, DOI: 10.1038/srep03669.
34 L. Feng, H. Vrubel, M. Bensimon and X. Hu, *Phys. Chem. Chem. Phys.*, 2014, **16**(13), 5917–5921, DOI: 10.1039/c4cp00482e.
35 H. Aziam, S. Indris, M. Knapp, H. Ehrenberg and I. Saadoune, *ChemElectroChem*, 2020, **7**, 3866–3873, DOI: 10.1002/celc.202001065.
36 M. Terlemezoglu, O. Surucu, M. Isik, N. M. Gasanly and M. Parlak, *Appl. Phys. A:Mater. Sci. Process.*, 2022, **128**(1), 1–6, DOI: 10.1007/s00339-021-05197-y.
37 J. Li, C. Xu, X. Li and Z. Su, *J. Phys.:Conf. Ser.*, 2021, **1759**(1), 012012, DOI: 10.1088/1742-6596/1759/1/012012.

38 M. Manikanta Kumar, R. Singh and C. R. Raj, *Chem.–Asian J.*, 2024, **19**(23), e202400684, DOI: 10.1002/asia.202400684.
39 T. K. Sahu, J. Saha, A. Anil, G. Salazar-Alvarez and M. Johnsson, *ACS Appl. Energy Mater.*, 2024, **7**(10), 4445–4453, DOI: 10.1021/acsaem.4c00386.
40 J. Saha, T. K. Sahu, J. Montero, A. Rydh, G. Salazar Alvarez and M. Johnsson, *ACS Appl. Energy Mater.*, 2025, **8**(15), 10868–10880, DOI: 10.1021/acsaem.5c00746.
41 T. Z. Fahidy, Hydrodynamic Models in Magnetoelectrolysis, *Electrochim. Acta*, 1973, **18**(8), 607–614, DOI: 10.1016/0013-4686(73)85026-1.
42 L. Elias and A. C. Hegde, *Electrocatalysis*, 2017, **8**(4), 375–382, DOI: 10.1007/s12678-017-0382-x.
43 O. Devos, O. Aaboubi, J. P. Chopart, A. Olivier, C. Gabrielli and B. Tribollet, *J. Phys. Chem. A*, 2000, **104**(7), 1544–1548, DOI: 10.1021/jp993696v.
44 Y. Zhang, C. Liang, J. Wu, H. Liu, B. Zhang, Z. Jiang, S. Li and P. Xu, *ACS Appl. Energy Mater.*, 2020, **3**(11), 10303–10316, DOI: 10.1021/acsaem.0c02104.